CFD MODELLING OF FLOW AND HEAT TRANSFER
IN INDUSTRIAL APPLICATIONS

Suhas V. PATANKAR

Department of Mechanical Engineering
University of Minnesota, Minneapolis, MN 55455, USA
and
Innovative Research, Inc., Plymouth, MN 55447, USA

ABSTRACT

This paper presents application of computational modelling to a number of problems of industrial importance. The problems include ventilation and fire spread in highway tunnels, chemical vapor infiltration for manufacturing fiber-reinforced composites, refining hearths used for elimination of impurities in high-performance alloys, and the ESR and VAR processes for remelting. The noteworthy physical and computational features of each problem are described and some selected results are shown along with comparison with measurements.

INTRODUCTION

Over the last thirty years, computational fluid dynamics and heat transfer have been increasingly used for a wide variety of engineering applications. In the beginning, the use of these techniques was customary only in the aerospace and nuclear fields. Subsequently, the use has spread to a variety of products, physical situations, and manufacturing processes. Some examples of interesting applications of computational modelling are: cooling of electronics systems, rotating and reciprocating machinery, furnaces and combustion chambers, chemical vapor deposition, plasma processing, refining hearths for alloys, and grain drying.

In such applications, computational modelling allows us to perform simulations of complex problems, investigate the effect of different design parameters, obtain detailed distributions of all relevant variables, and gain insight into the underlying physical processes. By a proper use of modelling, one can cut down on time-consuming and costly experiments and field measurements, avoid design by trial and error, obtain speedy results, and design better products and processes.

The purpose of this paper is to describe some selected applications of computational fluid dynamics and heat transfer to problems of industrial interest. In each case, the computational novelties are briefly outlined and some of the interesting results are presented.

The first problem deals with ventilation and fire spread in highway tunnels. It shows the validation of a computational model of modest complexity by comparison with extensive field measurements. The next problem deals with chemical vapor infiltration used for manufacturing fiber-reinforced composites. This problem presents a number of computational challenges. An interesting combination of models at the microscopic and macroscopic levels is used to address the problem without requiring excessive computing resources. The next problem involves refining hearths used for elimination of impurities in high-performance alloys. The computational model incorporates buoyancy and Marangoni forces,

melting/freezing, and particle tracking. Finally, the modelling of the ESR and VAR remelting processes is described.

TUNNEL VENTILATION

The problem considered. Fire spread, smoke movement, and ventilation in highway tunnels is an important problem of public safety. One approach for blowing the smoke out of the tunnel is to create a longitudinal flow using jets fans. Since measurements from an extensive test program conducted on Memorial Tunnel (Fig. 1) were available (Massachusetts Highway Department, 1995), a computational model was constructed and validated against the test data. This study is described in Massachusetts Highway Department (1999) and Karki, et al, (2000).
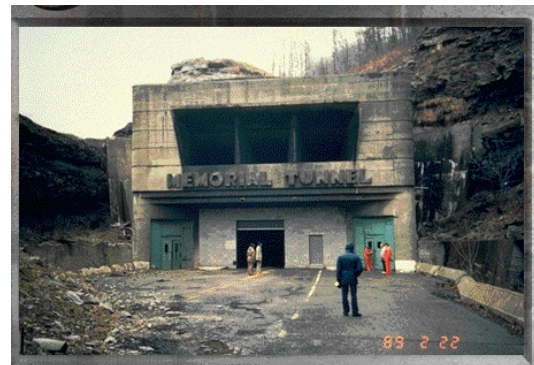

Figure 1. Memorial Tunnel in West Virginia

The computational model. The computations are based on the solution of three-dimensional equations for flow, temperature, and smoke concentration. The turbulence is handled by the k-ε model with appropriate source terms for turbulence production due to buoyancy. The fire is represented as a source of heat and mass, distributed in a region attributed to the fire. The same region also serves as a source of smoke concentration.

Jet fans are mounted on the ceiling of the tunnel as shown in Fig. 2. They are treated as volumetric flow devices and are modeled by appropriate sources and sinks of mass and momentum. The air jet issued by a jet fan entrains surrounding air and produces a longitudinal flow through the tunnel to drive the smoke out of the tunnel.

The sample results included in this paper pertain to the case of a 100 MW fire. Three minutes after the ignition, six jet fans were activated and maintained for 12 minutes; thereafter, one jet fan was deactivated.
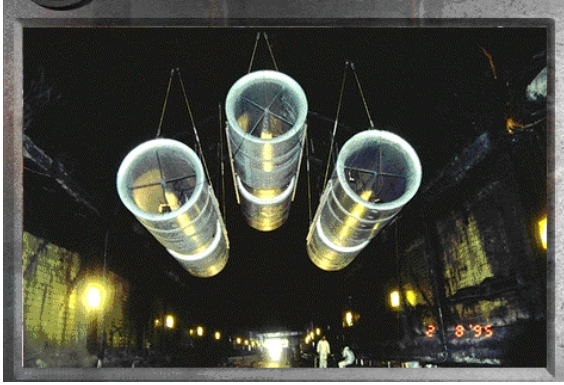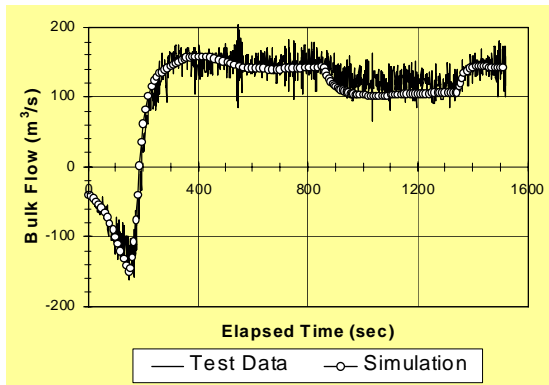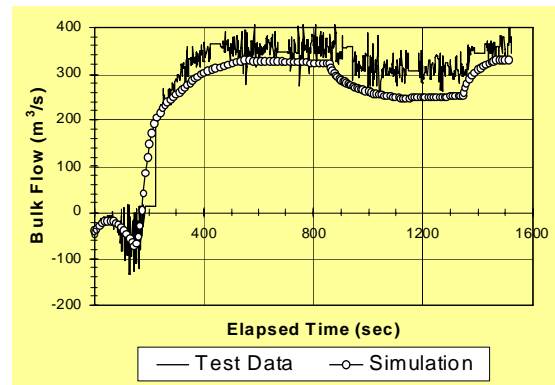
Figure 2. Jet fans mounted in the tunnel

Results for bulk flow. The total flow rate at two different longitudinal locations is plotted as a function of time in Fig. 3. The flow rate changes due to the buoyancy forces and the effect of the jet fans. The computed solution agrees very well with the measurements.

Distribution of temperature and smoke concentration.

Figures 4-6 show the contours of temperature and smoke distribution at three important instants in the process of fire spread and ventilation. Each figure includes the computed and measured temperature contours followed by the computed and measured *visibility* contours. Visibility is derived from the smoke concentration by using an empirical relation.

Figure 4 displays the condition before any jet fans are switched on. Because of a slight gradient in the tunnel, the fire and smoke preferentially move towards the left (north) end of the tunnel. Nearly the whole tunnel is filled with smoke. When the six jet fans are activated, they push the smoke out of the right (south) end of the tunnel. This condition is shown in Fig. 5. Figure 6 refers to the condition when only five jet fans are operating; they are sufficient to keep the smoke out but there is some evidence of "back-layering", i.e., the spread of a smoke layer upstream of the fire location.

The results presented in Figs. 4-6 show satisfactory agreement between the computation and measurement.
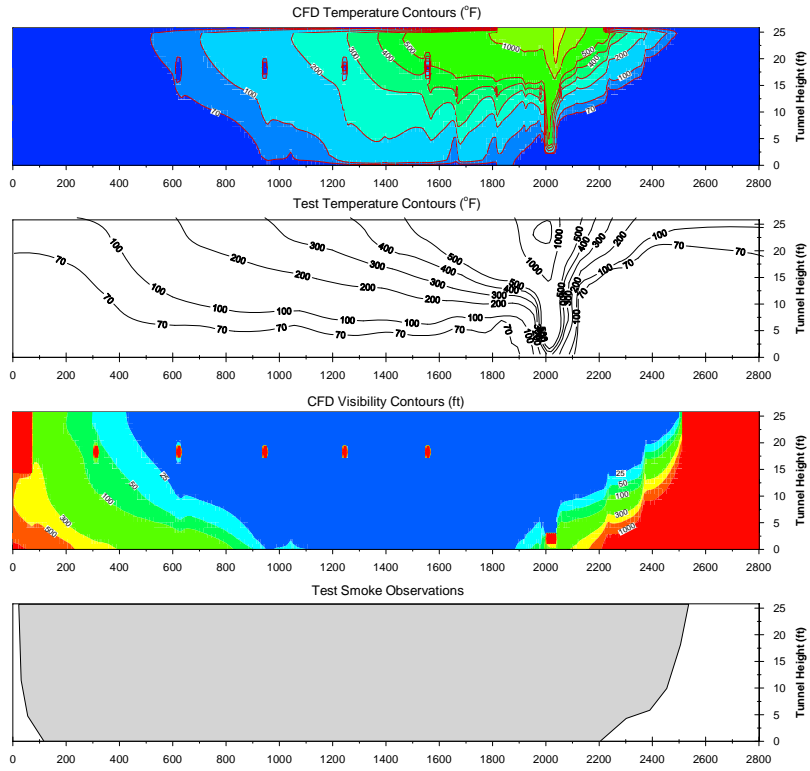

(a) 108 m North of fire

(b) 107 m South of fire

Figure 3. Total flow rate through the tunnel as a function of time

CFD Temperature Contours (°F)

Test Temperature Contours (°F)

CFD Visibility Contours (ft)

Test Smoke Observations

Figure 4. Distribution of temperature and smoke concentration at t=147 s (no jet fans on)

CFD Temperature Contours (°F)

Test Temperature Contours (°F)

CFD Visibility Contours (ft)
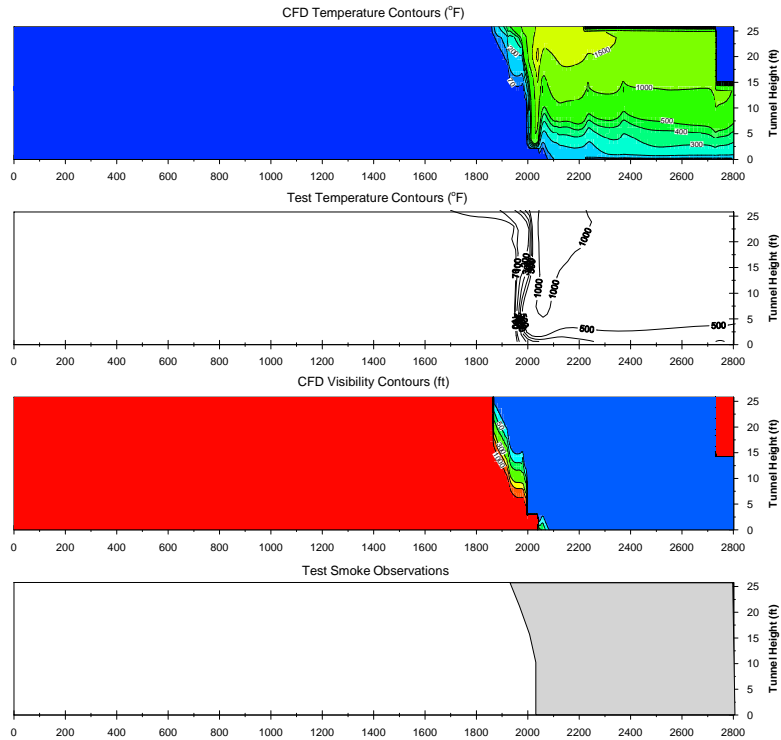
Test Smoke Observations

Figure 5. Distribution of temperature and smoke concentration at t=700 s (six jet fans on)
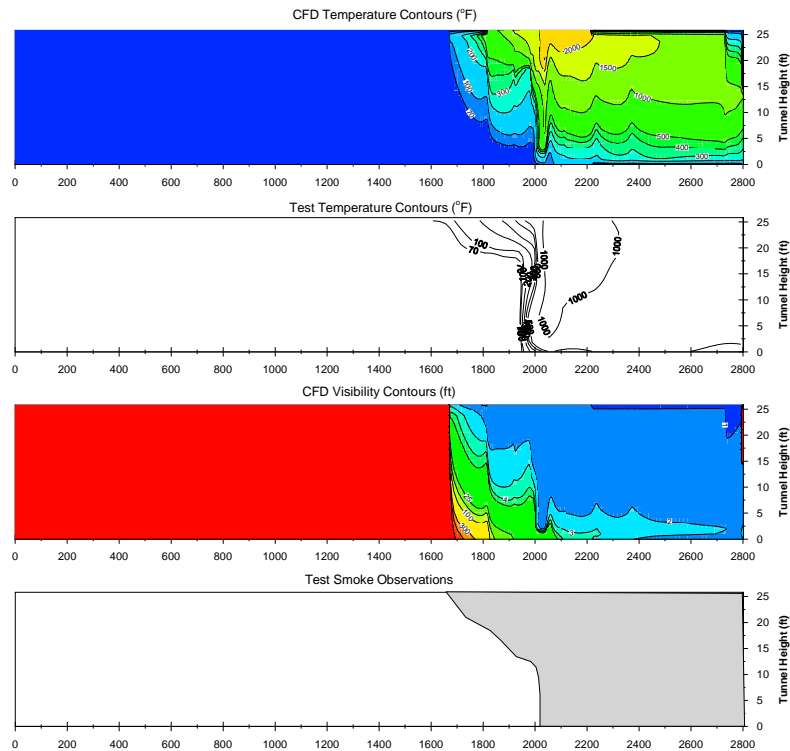
3

Figure 6. Distribution of temperature and smoke concentration at t=1000 s (five jet fans on)

CHEMICAL VAPOR INFILTRATION (CVI)

The manufacturing process. One possible method for building silicon-carbide fiber-matrix composites is to create a preform of layers of a fiber weave, pass a reactive gas such as CH_3SiCl_3 through the pores, and deposit silicon carbide on the fibers by a surface chemical reaction. This manufacturing process is called Chemical Vapor Infiltration (CVI). Whereas the process is capable of producing high-quality parts of final desired shapes, careful process control is needed. As the inter-fiber space gets filled up, the formation of inaccessible voids can lead to only partially densified material. Also, when large parts are made, a rapid densification at the outer boundaries can prevent any infiltration to the inner region.

The modelling challenge. The complete computational simulation of the CVI process presents the difficulty of two different scales. The fibers and the interspaces between them are only a few microns in size, while the finished parts may be many centimeters long. Further the process is time-dependent and the fibers grow with time due to deposition. Thus, to perform transient computations on the scale of the whole part while resolving the details around individual fibers of changing geometry is obviously beyond the reach of common computer resources. The problem can, however, be simplified by considering micro and macro models and quasi-steady behavior as described below.

The micro model. The main idea of this approach is to use the microscopic details of the fiber arrangements to characterize the *effective* properties of the resulting porous material and to calculate the deposition process in the whole part by using these properties. The fiber weaves are made like textile material with a regular fiber pattern. A typical weave is shown in Fig. 7. (The fibers

do not seem to have a circular cross section. Actually, they are fiber tows, which are bundles of many fibers. The resulting bundle may have an elliptical cross section.) The regularity of the pattern allows us to identify a unit cell, shown in Fig. 8, such that by repeating the cell the entire preform can be constructed. We also need to consider unit cells at different levels of densification, when the fiber tows have grown to a larger size. These are also shown in Fig. 8, where ϕ denotes the solid volume fraction or the degree of densification.
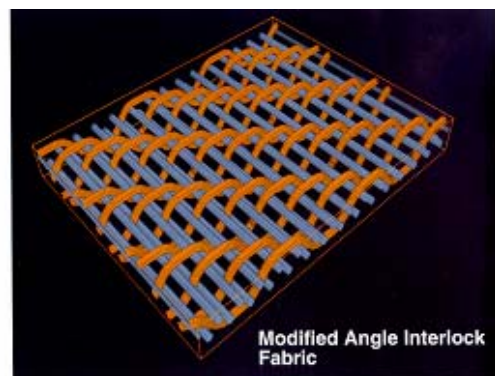

Figure 7. A typical weave used for fiber preforms

A unit cell can be analyzed, with a modest computational effort, to obtain the effective properties of the porous material. By imposing gradients of pressure, temperature, and concentration over the unit cell, we can obtain the corresponding fluid flow rate, heat flow rate, and diffusion flux and thus evaluate the *effective* permeability, conductivity, and diffusion coefficient for the material. These properties can be anisotropic. Further, they need to be calculated for the geometries that correspond to different levels of densification as shown

4

in Fig. 8. Representative results for the effective thermal conductivity are shown in Fig. 9 for a particular weave known as the 5-harness satin.
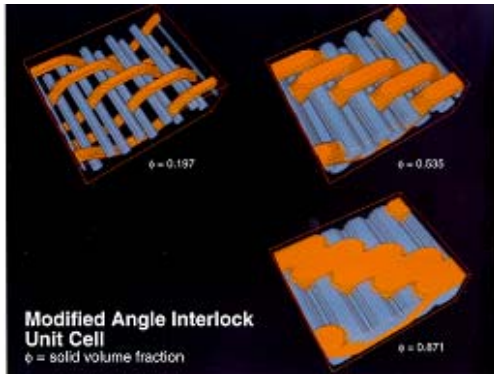

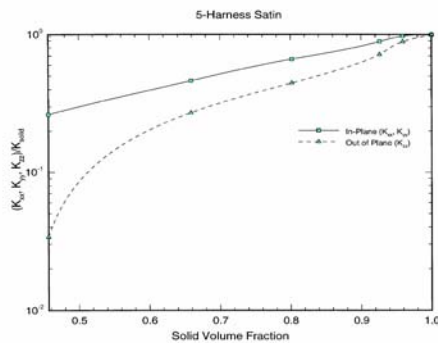**Figure 8**. Unit cells at different densification levels

Figure 9. Variation of effective thermal conductivity at different densification levels

The macro model. Once the porous material is characterized for different levels of densification, the CVI process can be modelled for the actual dimensions of the preform (without using a grid resolution of the size of the fibers). Although the real process is transient, the growth of the fibers is very slow and thus allows a quasi-steady formulation. For the initial undensified preform, the steady-state distributions of fluid flow, temperature,

and reactive-gas concentration can be calculated (based on the *effective* transport properties obtained in the micro model). This solution gives the local deposition rate of silicon carbide (which is nonuniform due to variations in temperature and reactive-gas concentration). It is then used to find the local level of densification (i.e., the solid volume fraction) after a finite time step. For this new geometry, another steady-state calculation is performed by using the local *effective* transport properties based on the local level of densification. The corresponding deposition rates are used to advance to the next instant of time. Thus, by using a succession of steady-state solutions, the progressive densification of the preform is predicted. The computation is continued until no further deposition can occur due to inaccessible voids or plugged boundaries.

Sample results. A simple application of the ideas described above is shown in Fig. 10 for a preform slab of certain thickness exposed to the reactive gas on its both surfaces. The densification profiles shown in Fig. 10 for different instants of time indicate that, as the reactive gas infiltrates into the preform and its concentration gets depleted, much less deposition occurs in the interior region. The final result is that, after the inter-fiber spaces at the faces of the preform get plugged up, the CVI process stops leaving the interior insufficiently densified. Since the chemical reaction rate depends on temperature, thermal gradients can be used to encourage and discourage densification in different regions.
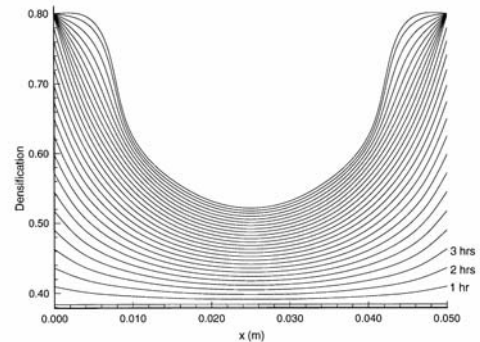

Figure 10. Densification profiles in a preform slab
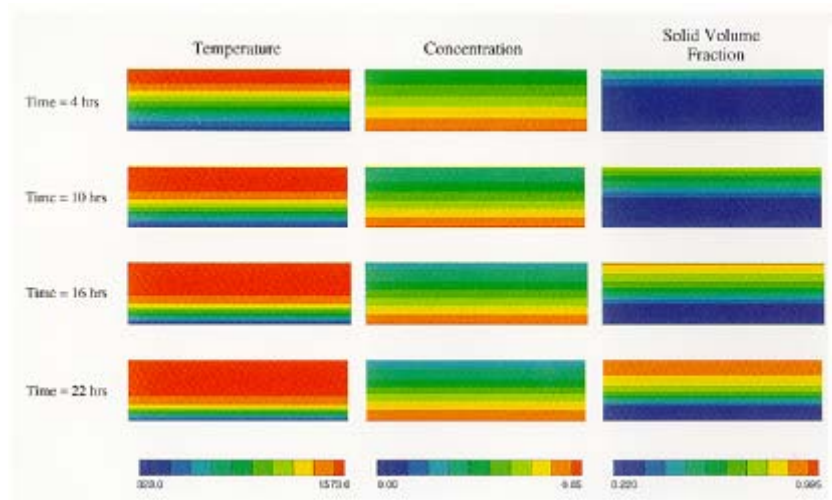

Figure 11. Densification process with a thermal gradient

Figure 11 shows the case of a rectangular preform exposed to the reactive gas on one face and maintained at a higher temperature on the opposite face to encourage early deposition there. The progression of the temperature and concentration fronts with time are shown along with the amount of densification achieved at different locations. The results for even simple problems like these show the difficulty of obtaining a uniform densification everywhere. More interesting results have also been obtained for complex geometries and boundary conditions, but are not shown here.

REFINING HEARTH

Refining of high-performance alloys. Aircraft engine parts are made from titanium alloys that must be ultra-pure. When titanium reacts with nitrogen, hard particles of titanium nitride are formed. If they are embedded in an ingot of the alloy, these "inclusions" form a weak spot, which can lead to the failure of a critical engine part. Some of the airplane accidents have been traced back to the presence of a single hard inclusion in the turbine disk. For this reason, the alloys used for these critical applications are refined and re-refined to achieve ultimate purity. One arrangement for the refining process is to use a refining hearth setup as shown in Fig. 12. The unrefined material is first melted in a melting hearth, it then flows into two successive refining hearths, and finally the refined metal is cast as an ingot. The material is contained in water-cooled crucibles but is kept molten by plasma torches or electron beam guns. As the metal flows through the refining hearths, any hard inclusion particles get a chance to dissolve in the surrounding liquid metal or get captured in the "mushy" region between the molten metal and the solid skull on the crucible wall.
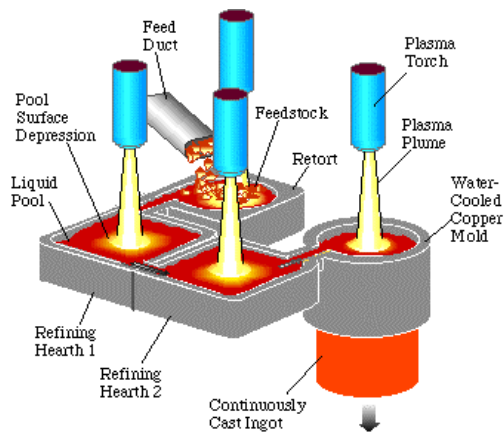

Figure 12. Schematic diagram for a refining hearth setup

Computational model. The flow and heat transfer in the refining hearth are influenced by buoyancy forces due to density variations and Marangoni forces due to the temperature-dependent surface tension at the surface of the molten pool. The Marangoni forces are quite strong and lead to a significant motion at the free surface. The flow is directed from the hot region to the cold region (i.e. away from the plasma torch) and thus helps in pushing the inclusions from the bulk of the liquid to the mushy zone, where they can be captured. The melting/freezing is calculated by using the enthalpy-porosity method of Brent, et al (1988).

Representative Results. The results for the hearth problem have been presented for the plasma hearth in Huang, et al (1999) and for the electron beam hearth in Kelkar, et al (1997). Some sample results are given here. The calculated pool shape of the liquid pool is shown in Fig. 13. The heating due to the plasma torch has to be such that the resulting pool shape gives sufficient residence time for the inclusions to dissolve, provides enough solid skull and mushy regions for the inclusions to get trapped, and leaves the inlet and outlet unfrozen for an unimpeded flow through the hearth. Figure 14 shows the distributions of temperature and velocity vectors on selected planes in the refining hearth. Based on the calculated flow field, trajectories of inclusion particles of various sizes and densities can be obtained and their fate determined in terms of dissolution, mushy-zone entrapment, or (the undesirable outcome of) passage into the cast ingot. No results for the particle trajectories are included in this paper for lack of space.
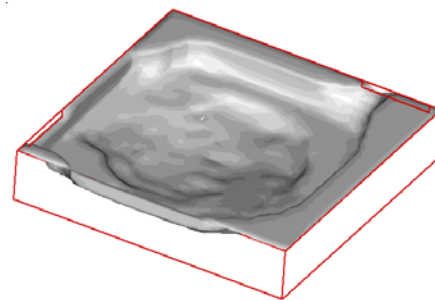

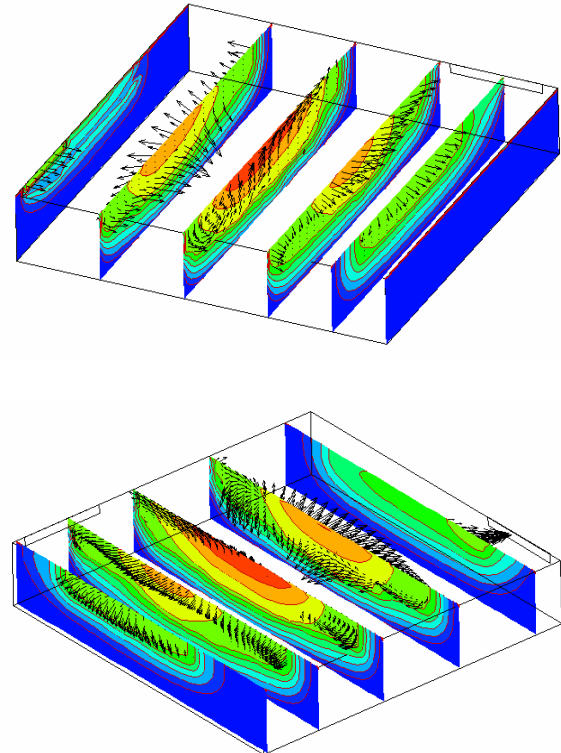**Figure 13.** Calculated pool shape for the refining hearth

Figure 14. Temperature fields and velocity vectors in the refining hearth

A comparison of predicted and measured pool shapes is shown in Fig. 15. With all the uncertainties in performing the measurements and the necessary simplifications in the computational model for this complex problem, the agreement is quite satisfactory.
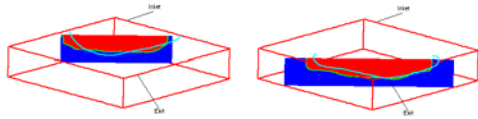

Figure 15. Comparison of calculated and measured pool shapes in the refining hearth

ESR AND VAR REMELTING PROCESSES

Production of high-performance alloys of Titanium, Nickel, and Steel involve use of Electroslag Remelting (ESR) and/or Vacuum Arc Remelting (VAR) for ensuring that the final ingots possess uniform composition and are defect free.

Computational models for the ESR and VAR processes should account for all the underlying physical phenomena, namely electromagnetic, fluid flow, heat transfer, phase change, and macrosegregation.

ESR Process. The computational model for the ESR includes the slag and the molten pool. The AC electromagnetics is analyzed by solving the magnetic diffusion equation with complex variables. Electromagnetic analysis predicts the distribution of Joule heating and Lorentz forces in the slag and the ingot regions. Turbulent flow in the slag and the molten pool, created by the combined action of buoyancy and Lorentz forces, is analyzed by using the k-ε turbulence model. The thermal boundary conditions in the slag-metal system account for the thickness of the slag skin and the ingot shrinkage at ingot-mould interface.

The model predicts all important aspects of the observed behavior namely skin effect for the radial current distribution in the ingot, the presence of a liquid-metal head below the slag, and the Vee-shaped molten pool (Kelkar et al., 2005). This is seen from Fig. 16 for the application of the model for an ESR process for Superalloy-718.

VAR Process. For the VAR process, the effect of the arc is considered by specifying the heat and mass fluxes and current density distributions on the ingot surface. The DC electromagnetics is analyzed to determine the distributions of current densities and Lorentz forces in the ingot. The angular motion caused by magnetic stirring and its effect on the in-plane velocity field are also considered. Equations for the transport of species concentrations that account for their selective rejection/absorption during solidification are solved to predict the distribution of the concentrations of the alloying elements in the entire ingot. The growth of the ingot is addressed by advancing the base plate through the computational grid and a special technique is used for the partially filled control volume containing the moving base plate (Kelkar et al., 2007). The model predicts the pool shape, flow in the molten pool, thermal history, and alloy concentrations within the growing ingot throughout the process. This is illustrated in Figs. 17-19 for the application of the model for a practical VAR process for Ti-64.
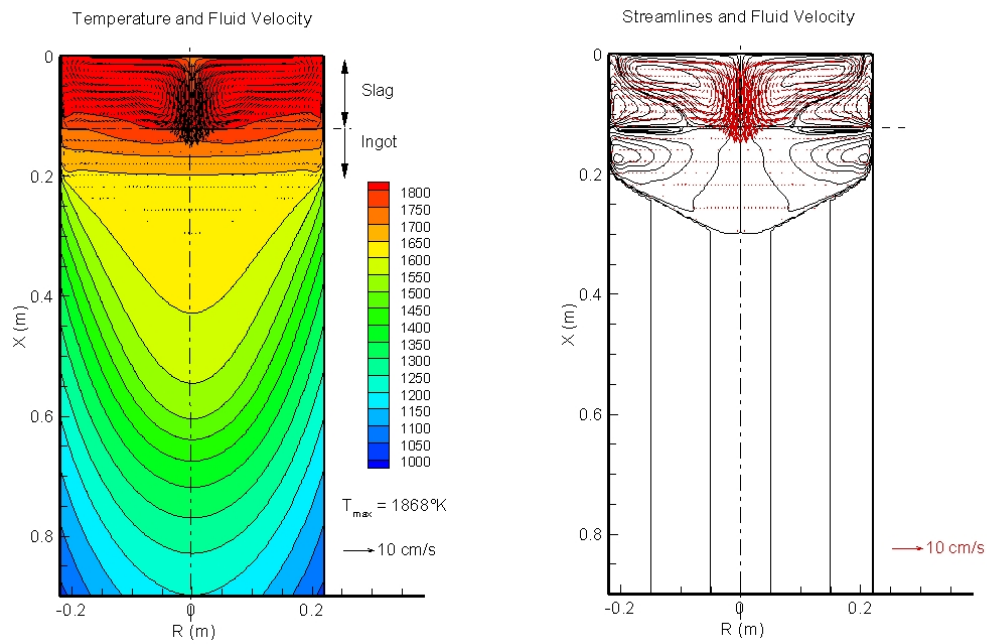
CLOSING REMARKS

Computational modelling of complex fluid flow and heat transfer has been described for four physical situations of practical interest. Each application involves a number of noteworthy computational and physical aspects. The computational models have been devised to capture the important physical processes and to minimize the computational effort. The results reveal many interesting physical effects and give satisfactory agreement with measurements.
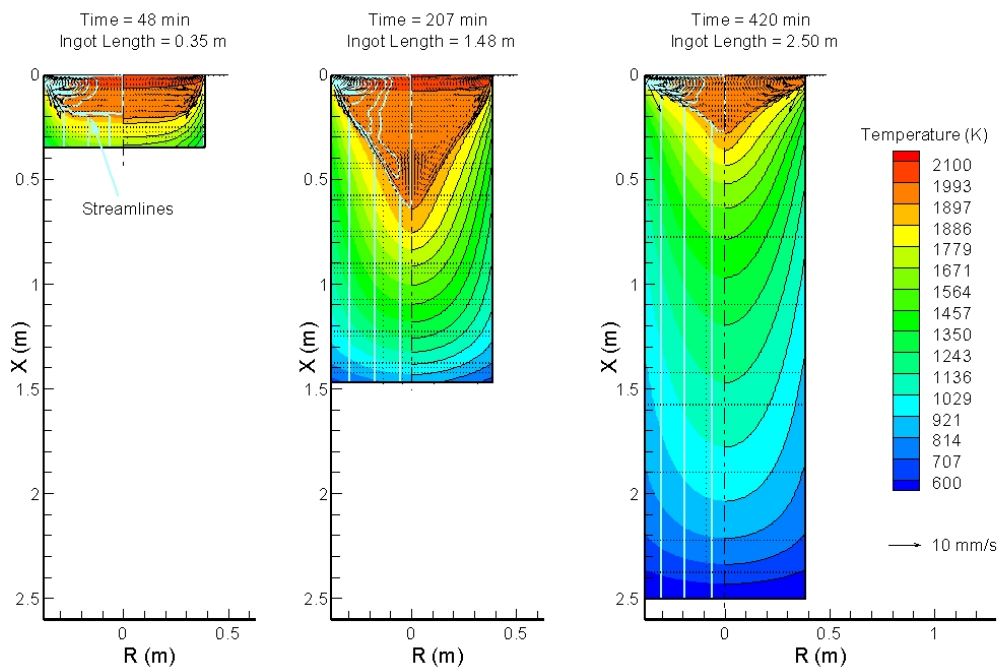
REFERENCES

BRENT, A.D., VOLLER, V.R., AND REID, K.J., (1988) "Enthalpy-Porosity Technique for Modeling Convection-Diffusion Phase Change: Application to Melting of a Pure Metal," Numerical Heat Transfer, Vol. 13, pp. 297-318, 1988.

HUANG, X., CHOU, J.S., AND PANG, Y.,(1999) "Modeling of Plasma Arc Cold Hearth Melting and Refining of Ti Alloys," *Proceedings of the 1999 International Symposium on Liquid Metal Processing and Casting*, pp. 224-243, 1999.

KARKI, K.C., ROSENBLUTH, E., PATANKAR, S.V., AND LEVY, S. (2000) "CFD Model for Jet Fan Ventilation Systems," *10th Symposium on Aerodynamics and Ventilation of Vehicle Tunnels*, BHR Group 2000 Vehicle Tunnels, pp. 355-380, 2000.

KELKAR K.M., PATANKAR S.V., MITCHELL A., (2005) "Computational Modeling of the Electroslag Remelting (ESR) Process Used for the Production of Ingots of High-Performance Alloys," Proceedings of the Liquid Metal Processing and Casting Conference, Santa Fe, NM, USA, September 18-21, 2005, pp. 137-144.

KELKAR K.M., PATANKAR S.V., MITCHELL A., (2007) "Computational Modeling of the VAR Remelting Process Used for the Production of Titanium Alloys," To be presented at the Ti-2007 Conference, Japan, 2007.

KELKAR, K.M., PATANKAR, S.V., AND SRIVATSA, S.K.,(1997) "Mathematical Modeling of the Electron Beam Cold Hearth Refining of Titanium Alloys," *Proceedings of the Electron Beam Melting and Refining Conference*, State of the Art 1997, pp. 238-251, 1997.

Massachusetts Highway Department And Bechtel/Parsons Brinckerhoff, (1995) *Memorial Tunnel Fire Test Ventilation Program – Test Report*, 1995.

Massachusetts Highway Department/Federalhighway Administration, (1999) *Memorial Tunnel Fire Ventilation Test Program, Phase IV Report*, 1999.
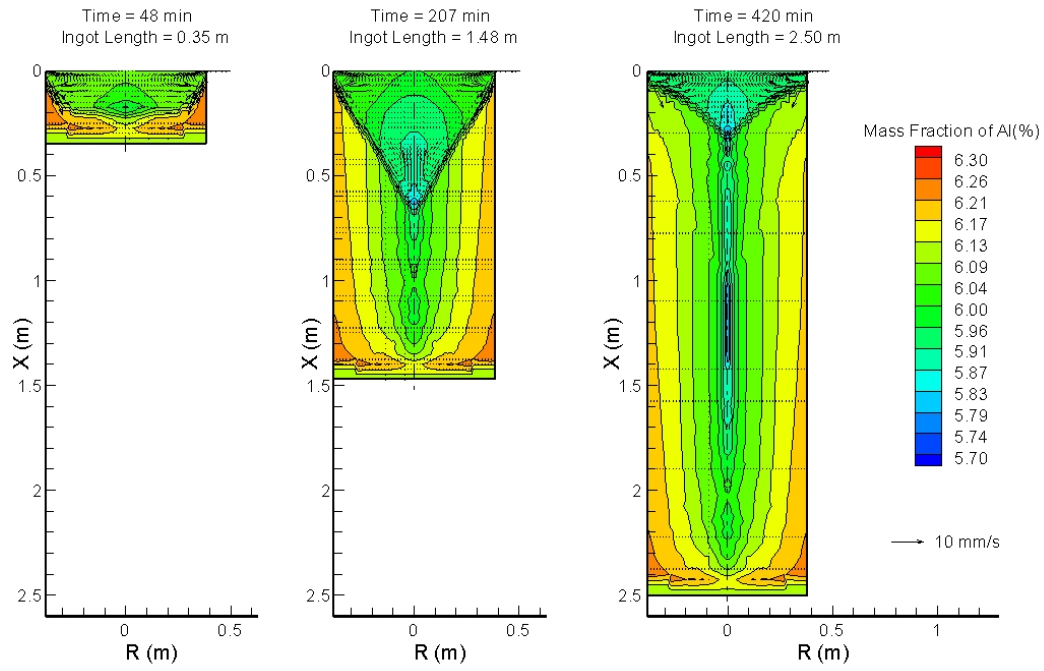
Flow and Temperature Fields Under Steady State Conditions in a Practical ESR Process for Alloy IN-718
Slag Height = 120 mm, Electrode Diameter = 339 mm, Ingot Diameter = 440 mm
Total Current = 13.5 kAmp, AC Frequency = 60 Hz, Power = 360 kW, Melt Rate = 6.75 kg/min

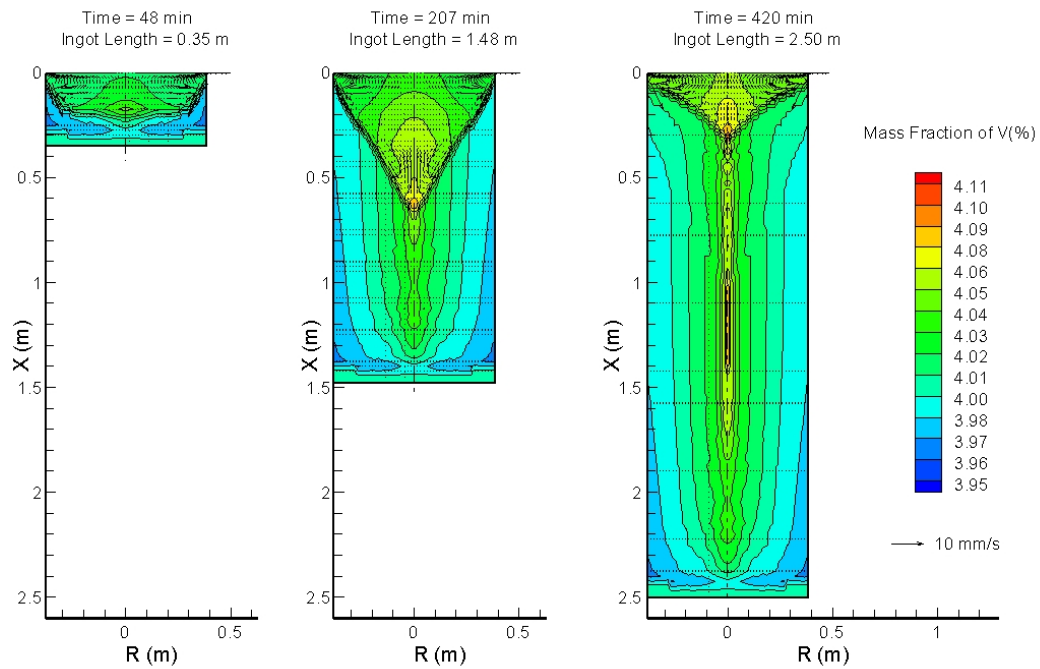**Figure 16.** Simulation results for a practical ESR remelting process.

Flow in the Pool and Temperature Distribution During a Practical VAR Process for Ti-64 Alloy
Solidus Temperature = 1868 K, Liquidus Temperature = 1898 K
Ingot Diamater = 760 mm, Electrode Diameter = 660 mm

Figure 17. Flow and temperature in a growing ingot in a VAR process.

Distribution of Aluminum Mass Fraction During a Practical VAR Process for Ti-64 Alloy
Mass Fraction of Aluminum in the Electrode = 6.125%
Ingot Diamater = 760 mm, Electrode Diameter = 660 mm

Figure 18. Calculated concentrations of Aluminum in a VAR ingot.

Distribution of Vanadium Mass Fraction During a Practical VAR Process for Ti-64 Alloy
Mass Fraction of Vanadium in the Electrode = 4%
Ingot Diamater = 760 mm, Electrode Diameter = 660 mm

Figure 19. Calculated concentrations of Vanadium in a VAR ingot.